Liquid Metal Batteries

Norbert Weber and Tom Weier

Abstract Liquid metal batteries (LMBs) are introduced as future candidates for grid scale electricity storage. Their completely liquid cell interior entails a prominent role of fluid mechanics to understand and model their behaviour. We describe the equations used to compute electrochemical reactions, heat and mass transfer, electromagnetic fields, and fluid flow and explain the simplifications that can be made in the case of LMBs. The implementation of solution algorithms in OpenFOAM pertaining to domain coupling, multiphase simulations, mesh mapping, and operator discretisation are discussed in detail and accompanied by example code.

1 Introduction

Liquid metal batteries (LMBs) are high temperature electricity storage devices. They consist of a low density molten alkaline or alkaline earth metal as the negative electrode (anode), a high density post-transition metal or metalloid as the positive electrode (cathode), and a fused salt of intermediate density as the ionic conductor. The three liquid layers arrange themselves into a stable density stratification as sketched in Fig. 1a by virtue of the immiscibility of the two metals with the salt.

LMBs possess a number of properties that make them attractive candidates for grid electricity storage. With the growing importance of the latter, research on LMBs that had ceased after an active period in the 1960s (Cairns and Shimotake 1969) was revived at the beginning of the 21st century (Kim et al. 2013). Current densities in LMBs are very high with typical values of around 1 A/cm^2. Structure degradation,

Supplementary Information The online version contains supplementary material available at https://doi.org/10.1007/978-3-030-92178-1_7.

N. Weber (✉) · T. Weier
Helmholtz-Zentrum Dresden - Rossendorf, 01328 Dresden, Germany
e-mail: norbert.weber@hzdr.de

T. Weier
e-mail: t.weier@hzdr.de

S. Beale and W. Lehnert (eds.), *Electrochemical Cell Calculations with OpenFOAM*,
Lecture Notes in Energy 42, https://doi.org/10.1007/978-3-030-92178-1_7

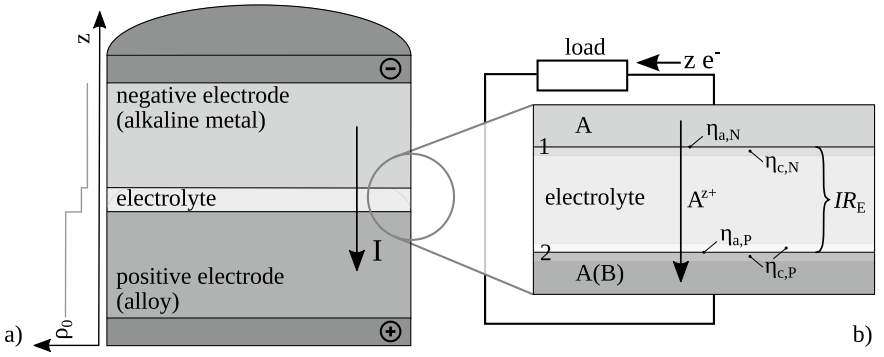

Fig. 1 Sketch of a liquid metal battery with idealised density distribution at equilibrium (**a**) and zoom of the interfacial regions with typical overvoltages (**b**)

one of the major problems causing capacity fade and failure of batteries with solid electrodes, is absent due to the liquid state of the active materials. LMBs can be composed from a variety of elements allowing the selection of abundant and economic ones. The simple construction of the cells enables scaling on the cell level up to potentially very large dimensions like those common in aluminium refinement and electrolysis.

Fluid mechanics has a major role to play in the design and analysis of LMBs due to the fully liquid cell interior. Electric currents, magnetic fields, and heat and mass transfer are tightly coupled with the cells' electrochemistry. Fluid flow can be induced by a number of mechanisms with a subset compiled in Table 1. They are briefly touched upon in the following and discussed in detail by Kelley and Weier (2018).

Electric current flow leads to a strong heating of the electrolyte since its electrical conductivity is with $\mathcal{O}(100)$ S/m much smaller than that of the electrode metals with typically $\mathcal{O}(10^6)$ S/m. The heat source in the middle of the cell drives intense natural convection in the electrolyte itself and—to a lesser extent—in the negative electrode above (Shen and Zikanov 2016; Personnettaz et al. 2018). Marangoni convection due to temperature and concentration differences can be expected to occur mainly in the electrolyte at the interfaces with the electrodes (Köllner et al. 2017; Weier et al. 2017).

At discharge, the anode metal is alloyed into the positive electrode; during charging, this process is reversed. The large density contrast between the anode and cathode metals causes strong density gradients in the positive electrode during charge and discharge. These gradients are stable during discharge but unstable during charge, inhibiting or driving solutal convection in the positive electrode, respectively (Personnettaz et al. 2019; Herreman et al. 2020; Personnettaz et al. 2020).

Finally, electromagnetic effects of the strong total currents that result from the high current densities in large cells can cause fluid flow. The Tayler instability (TI) (Weber et al. 2013) is a kink-type instability akin to the z-pinch known from plasma physics.

Table 1 Convection types to be expected in liquid metal batteries

Convection type	Typical location	Cause
Tayler instability	Negative electrode	Electromagnetic
Metal pad role instability	Interfaces	Electromagnetic
Electro-vortex flows	Electrodes	Electromagnetic
heat driven convection	Electrolyte	Temperature gradient
	Negative electrode	Temperature gradient
Marangoni convection (thermal)	Electrolyte at both interfaces	Temperature gradient
	Electrodes at both interfaces	Temperature gradient
Marangoni convection (solutal)	Electrolyte at both interfaces	Concentration gradient
	Positive electrode at interface	Concentration gradient
Solutal convection	Positive electrode	Concentration gradient

For total currents above a few kA the TI will occur in the negative electrode first due to its material properties. While even perfectly homogeneous current density distributions are subject to the TI, changes in a conductors cross section that are technically unavoidable lead to radial current density components and rotational Lorentz forces. The latter produce so-called electro-vortex flows. These flows might be weak, but there is no need to exceed a threshold current for them to be present.

The two interfaces between electrodes and electrolyte may develop interfacial waves (Weber et al. 2017) similar to those observed in aluminium reduction cells (ARCs). Large amplitude waves could short circuit the cell and should therefore be avoided. Unlike ARCs, LMBs posses two fluid-fluid interfaces that may interact, leading to a richer dynamics (Horstmann et al. 2017) compared to the single interface case.

The cell voltage E of an LMB under current flow I depends on the open circuit voltage E_{OC} and the sum of overvoltages η:

$$E = E_{\mathrm{OC}} \pm (I R_{\mathrm{E}} + \eta_{\mathrm{a,\,N}} + \eta_{\mathrm{c,\,N}} + \eta_{\mathrm{a,\,P}} + \eta_{\mathrm{c,\,P}}), \tag{1}$$

with the activation overvoltages (subscript a) $\eta_{\mathrm{a,\,N}}$, $\eta_{\mathrm{a,\,P}}$ at the positive (subscript P) and negative (subscript N) electrodes. The corresponding mass transfer overvoltages (subscript c) are denoted by $\eta_{\mathrm{c,\,N}}$, $\eta_{\mathrm{c,\,P}}$ and the ohmic voltage loss is due to the resistance of the electrolyte R_{E}. The plus sign in Eq. (1) applies to charge, the minus sign to discharge. The open circuit voltage itself

$$E_{\mathrm{OC}} = -\frac{RT}{zF} \ln a_{\mathrm{A(B)}} \tag{2}$$

depends on the activity $a_{\mathrm{A(B)}}$ of the negative electrode material A in the positive electrode material B. R is the ideal gas constant, T the temperature, z the valence, and F

the Faraday constant (see Sect. 2.1 for details). Charge transfer at the liquid-liquid interface is very fast at the high operating temperatures (300–600 °C). Therefore the activation overvoltages are negligible. The electrolyte is the source of the ohmic voltage drop $I R_\mathrm{E}$ that is in most cases the largest contribution to the total overvoltage. Mass transfer limitations in the electrolyte may arise, if salt mixtures with different cations are used. However, this brings about a number of other detrimental effects and is therefore avoided in most cases. Irrespective of the salt mixture, heat release in the electrolyte should generate intense convection and sufficient mixing so that no substantial mass transfer overvoltages are to be expected in the electrolyte. The situation is, however, different for the positive electrode. Since it is the activity of A(B) directly at the interface to the electrolyte that determines E_OC, mass transfer in the positive electrode is crucial for cell performance. Comparing the contribution of solutal and thermal gradients to the alloy density differences reveals (Kelley and Weier 2018; Personnettaz et al. 2019) that the influence of compositional gradients far outweighs that of temperature. As mentioned above, strong solutal convection appears during charge, but diffusion dominates mass transfer during discharge and limits cell performance. The aforementioned electro-vortex flows are a good candidate to counteract this stable density stratification and to improve mixing in the positive electrode (Weber et al. 2018) during discharge.

2 Physical and Numerical Model

2.1 Electrochemistry

When discharging an LMB, metal A is oxidised at the anode-electrolyte interface as

$$\mathrm{A} \longrightarrow \mathrm{A}^{z+} + z\mathrm{e}^-,$$

crosses the electrolyte and is reduced at the cathode-electrolyte interface as

$$\mathrm{A}^{z+} + z\mathrm{e}^- \longrightarrow \mathrm{A(B)}$$

where it dissolves into metal B (Kim et al. 2013). For clarity, we will focus in the following on the well investigated Li||Bi cell, where Li dissolves into Bi. There, the number of exchanged electrons is $z = 1$.

From a macroscopic point of view, the electric potential will jump at both interfaces of an LMB—as illustrated in Fig. 2.

The cell current will always drive flow in the liquid electrodes—e.g. by heating or electromagnetic forces (Ashour et al. 2018; Weber et al. 2018). Therefore, it is not sufficient to model only the scalar value of the cell current: we need to know its three-dimensional distribution, as well (Weber et al. 2019, 2020). This is quite

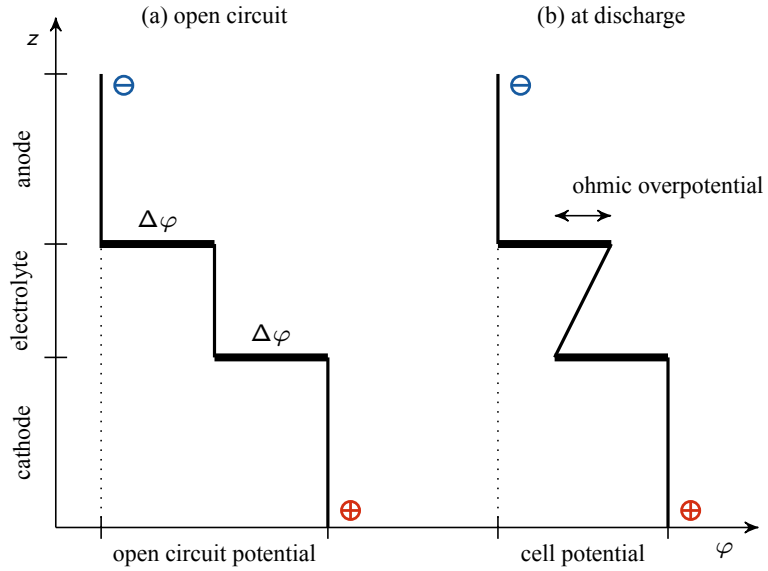

Fig. 2 Vertical profile of the electric potential in an LMB at open circuit (**a**) and discharge (**b**) (Weber et al. 2019)

remarkable, because for classic batteries it is sufficient to find the overpotentials in, or at the electrolyte—but not the current distribution in the electrodes.

In a first step, the electric potential φ will be solved as

$$\nabla \cdot \sigma \nabla \varphi = 0, \tag{3}$$

where σ denotes the ohmic or ionic conductivity. The potential jumps at the two interfaces are embedded into the Laplace operator, and are defined by the Nernst equation as

$$\Delta\varphi = -\frac{RT}{zF} \ln\left(\frac{a_{\text{ox}}}{a_{\text{red}}}\right), \tag{4}$$

with R, T, F and a denoting the Universal gas constant, temperature, Faraday constant and chemical activity of the oxidated and reduces species. Finally, the current density $\boldsymbol{j}$ is computed as

$$\boldsymbol{j} = -\sigma \nabla \varphi. \tag{5}$$

Note that LMBs are simple concentration cells. Their cell voltage is therefore simply defined by the activity of one metal in the other metal.

Practical Advice

In a Li|LiCl-LiF|Bi LMB, the activity of Li^+ in LiCl-LiF is not known. In that case, the potential jump might be applied only at the bottom interface, computing its magnitude as $\Delta\varphi = -\frac{RT}{zF} \ln\left(a_{\mathrm{Li(Bi)}}\right)$. Even simpler, measured values of the open-circuit potential of a concentration cell can be fitted over concentration, and its value applied directly as potential jump at the electrolyte-cathode interface.

2.2 Mass Transfer

The potential jump at the interface depends on the activity—or concentration—of Li in Bi. Consequently, we need to model how Li dissolves into Bi in order to compute the cell voltage. We solve the diffusion-advection equation (Personnettaz et al. 2019, 2020)

$$\frac{\partial}{\partial t}\gamma + \nabla \cdot (\boldsymbol{u}\gamma) = \nabla \cdot (D\nabla\gamma) \tag{6}$$

for the mass concentration γ of Li, with t denoting time, $\boldsymbol{u}$ velocity and D the diffusion coefficient of Li in Bi. Although the density difference between Li and Bi is extreme, the Oberbeck-Boussinesq approximation is typically used to model solutal convection in LMBs. The body force caused by the concentration (i.e. density) gradients may be computed as

$$\boldsymbol{f} = \rho\boldsymbol{g} = \rho_0(1 - \beta_\gamma(\gamma - \gamma_0))\boldsymbol{g}, \tag{7}$$

where γ_0 denotes a reference concentration, $\boldsymbol{g}$ gravity, ρ_0 the reference density and β_γ the volumetric expansion coefficient. The amount of Li entering the positive electrode is proportional to the current density, and can be computed using Faraday's law. The normal gradient of the Li mass concentration at the interface is then

$$\nabla\gamma \cdot \boldsymbol{n} = -\frac{\boldsymbol{j}M}{zFD} \cdot \boldsymbol{n} \tag{8}$$

with M denoting the molar mass of Li and $\boldsymbol{n}$ the surface normal vector. Typical current densities for LMBs are in the order of 0.2-0.3 A/cm^2, but may reach even 1 A/cm^2.

Mass vs. Molar Concentration and Fraction

It is very much recommended to use mass concentration as primary variable for the diffusion-advection equation. In its original form, Fick's second law of diffusion reads

$$\frac{\partial c}{\partial t} = D\Delta c, \tag{9}$$

with c denoting the molar concentration in mol/m^3. Multiplying Fick's law by the molar mass of Li leads to

$$\frac{\partial \gamma}{\partial t} = D\Delta \gamma. \tag{10}$$

The mass concentration γ can be expressed by the mass fraction w and the density of the mixture ρ as $\gamma = w \cdot \rho$ which leads using the product rule to

$$\rho \frac{\partial w}{\partial t} + w \frac{\partial \rho}{\partial t} = D\rho\Delta w + Dw\Delta\rho. \tag{11}$$

As the density changes considerably when alloying Li into Bi, the terms $w\frac{\partial \rho}{\partial t}$ and $Dw\Delta\rho$ are not zero!

The Navier-Stokes equations describe how fast mass is transported, i.e. we use mass-averaged velocity. Alternatively, we could define a molar-averaged velocity, describing how fast the *amount* of Li and Bi is transported. When adding Li into Bi, the total amount, but also the mass of the mixture will change. If the change of the amount of substance and the density are linearly related to each other, the mass- and molar-averaged velocity are equal. This is, however, not the case for liquid metal batteries: when adding Li to Bi, the small Li atoms will intercalate between the large Bi atoms. While the total amount of substance changes considerably, density changes only slightly. Consequently, we need to use mass concentration as primary variable, because our velocity is always mass-averaged (Bird et al. 1960).

2.3 Flow Simulation

Convection in the liquid phases is modelled by solving the incompressible Navier-Stokes equations (Weber et al. 2018)

$$\frac{\partial(\rho \boldsymbol{u})}{\partial t} + \nabla \cdot (\rho \boldsymbol{u}\boldsymbol{u}) = -\nabla p + \nabla \cdot (\rho\nu(\nabla \boldsymbol{u} + (\nabla \boldsymbol{u})^{\mathsf{T}})) + \sum \boldsymbol{f}, \tag{12}$$

$$\nabla \cdot \boldsymbol{u} = 0, \tag{13}$$

with p denoting the pressure, ν the kinematic viscosity and $\boldsymbol{f}$ an arbitrary body force, such as gravitation or a Lorentz force. The equation system is solved using the PISO algorithm by first estimating a velocity. After solving a Poisson equation for the pressure, the velocity is corrected ensuring $\nabla \cdot \boldsymbol{u} = 0$. In certain cases, such as multiphase simulation or with thermal convection, it is better to switch off the momentum predictor in the *fvSolution* dictionary. Then, the velocity of the old time

step is used directly as estimate for the new velocity. The corrector step, i.e. the Poisson equation for pressure, should always be solved at least twice in order to ensure convergence.

Simplifications for Single Phase Flow

When simulating a single phase, the equation is usually divided by the constant density ρ. Assuming further the kinematic viscosity to be constant, the stress tensor can be simplified as

$$\nabla \cdot \rho\nu \left(\nabla \boldsymbol{u} + \nabla \boldsymbol{u}^{\mathsf{T}}\right) = \nabla \cdot (\rho\nu \nabla \boldsymbol{u}) + \nabla \boldsymbol{u} \cdot \nabla (\rho\nu) = \nabla \cdot (\rho\nu \nabla \boldsymbol{u}),$$

because $\nabla (\rho\nu) = 0$.

2.4 Heat Transfer and Thermal Convection

The temperature distribution in the cell is determined by solving the energy equation

$$c_p \left(\frac{\partial \rho T}{\partial t} + \nabla \cdot (\rho T \boldsymbol{u}) \right) = \nabla \cdot \lambda \nabla T + \frac{j^2}{\sigma} + \dot{Q}, \tag{14}$$

with c_p denoting the isobaric heat capacity, λ the thermal conductivity and j^2/σ the ohmic heat source. Additional heat sources $\dot{Q}$—such as the electrochemical heat due to the reaction—are sometimes included, as well (Personnettaz et al. 2018).

Thermal convection is modelled using the Oberbeck-Boussinesq approximation. The gravitational force is defined as

$$\boldsymbol{f} = \rho \boldsymbol{g} = \rho_0 (1 - \beta (T - T_0)) \boldsymbol{g}, \tag{15}$$

with β denoting the thermal expansion coefficient and T_0 the reference temperature. The part of the force which can be expressed as a gradient does not drive a flow. In order to reduce numerical errors, it is therefore included into the pressure gradient by defining a modified pressure as (Rusche 2002)

$$p_{\mathrm{d}} = p - \rho \boldsymbol{g} \cdot \boldsymbol{x}, \tag{16}$$

where $\boldsymbol{x}$ denotes the position vector. The gradient of the pressure becomes then

$$\nabla p = \nabla p_{\mathrm{d}} + \rho \boldsymbol{g} + \boldsymbol{g} \cdot \boldsymbol{x} \nabla \rho, \tag{17}$$

and $\rho \boldsymbol{g}$ disappears from the Navier-Stokes equation.

The Oberbeck-Boussinesq Aroximation

The Oberbeck-Boussinesq approximation is based on three assumptions (Gray and Giorgini, 1976):

- heating due to viscous dissipation is assumed to be negligible
- all material properties except density do not depend on temperature
- density changes are solely taken into account in the gravitational term

After choosing an allowed error ε, the admissible temperature difference in the simulation can roughly be estimated as

$$\Delta T = \frac{\varepsilon}{\beta}. \tag{18}$$

2.5 *Magnetohydrodynamics*

Magnetohydynamic effects can drive fluid flow by the Lorentz force

$$\boldsymbol{f} = \boldsymbol{j} \times \boldsymbol{b}, \tag{19}$$

i.e. by the cross-product of the current density and a magnetic field. The current density is determined – similar to Eqn. 3 – by first solving the Poisson equation

$$\nabla \cdot \sigma \nabla \varphi = \nabla \cdot \sigma (\boldsymbol{u} \times \boldsymbol{B}), \tag{20}$$

and then computing

$$\boldsymbol{j} = -\sigma \nabla \varphi + \sigma (\boldsymbol{u} \times \boldsymbol{B}) - \sigma \frac{\partial \boldsymbol{a}}{\partial t}, \tag{21}$$

with $\boldsymbol{a}$ denoting the vector potential. Simulating only direct currents, the last term of Eq. 21 can safely be neglected (Weber et al. 2013). The magnetic field may then be obtained by solving the quasi-static induction equation

$$0 = \frac{1}{\sigma \mu_0} \Delta \boldsymbol{b} + \nabla \times (\boldsymbol{u} \times \boldsymbol{b}) \tag{22}$$

with μ_0 denoting the vacuum permeability. The boundary conditions for the magnetic field are obtained from Biot-Savart's law as (Weber et al. 2015)

$$\boldsymbol{b}(\boldsymbol{r}) = \frac{\mu_0}{4\pi} \int \frac{\boldsymbol{j}(\boldsymbol{r}') \times (\boldsymbol{r} - \boldsymbol{r}')}{|\boldsymbol{r} - \boldsymbol{r}'|^3} dV', \tag{23}$$

where $\boldsymbol{r}$ denotes the coordinate vector of the magnetic field, $\boldsymbol{r}'$ of the current density and dV' the cell volume.

Alternatively, a transport equation for the vector potential may be solved as

$$0 = \Delta \boldsymbol{a} + \mu \boldsymbol{j} \tag{24}$$

with the boundary conditions obtained by Green's identity (Weber et al. 2018)

$$\boldsymbol{a}(\boldsymbol{r}) = \frac{\mu_0}{4\pi} \int \frac{\boldsymbol{j}(\boldsymbol{r}')}{|\boldsymbol{r} - \boldsymbol{r}'|} dV'. \tag{25}$$

Finally, the magnetic field is obtained as

$$\boldsymbol{b} = \nabla \times \boldsymbol{a}. \tag{26}$$

Practical Advice

Usually, large parts of the Lorentz force can be expressed as a pressure gradient, and therefore drive no flow. However, these large gradients can lead to considerable numerical errors. It is therefore highly recommended to avoid non-orthogonal cells. Computing the magnetic field directly—and not via the vector potential—is slightly slower. However, it is more accurate, because we do not need to compute an additional rotation ($\boldsymbol{b} = \nabla \times \boldsymbol{a}$). Finally, those parts of the Lorentz force, which can be expressed as a pressure gradient, should whenever possible be included into a modified pressure.

3 Domain Coupling

In many cases simulating a single electrode of the LMB is sufficient. Then, the equations can be considerably simplified, e.g. by diving them by the constant material properties. However, in certain cases it is necessary to simulate the full battery. Coupling non-deformable regions, like the battery housing with a liquid electrode, we will denote as "region coupling" in the following. Multiphase models describe how to simulate the interaction of the three deformable liquid layers as illustrated in Fig. 3.

3.1 Multiphase Simulation

Multiphase simulations are required to model the deformation of the interfaces between electrodes and electrolyte. The solver is based on the OpenFOAM standard solver *multiphaseInterFoam* using the volume of fluid method (Rusche 2002).

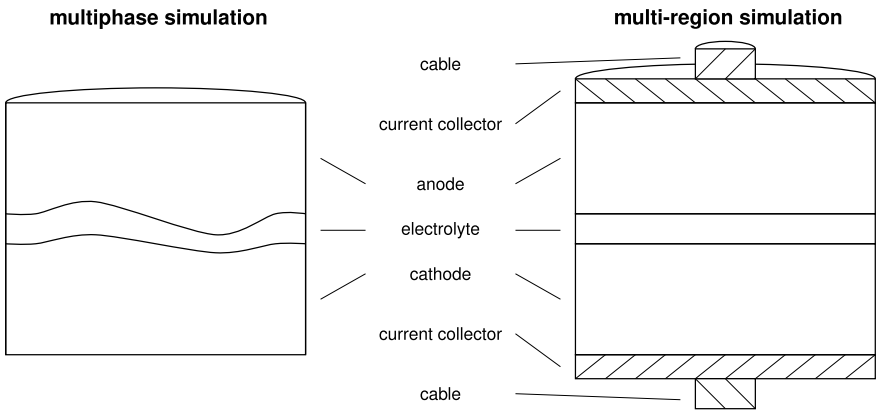

Fig. 3 While multiphase simulation can model the deformation of the interfaces between the electrodes and the electrolyte (left), multi-region modelling allows coupling of the current collectors and cables with the battery (right)

The volumetric phase fractions α_i describe the volume of a single phase in each computational cell. After solving the Navier-Stokes equations, the phase fractions α_i are solved as

$$\frac{\partial \alpha_i}{\partial t} + \nabla \cdot (\alpha_i \boldsymbol{u}) = 0. \tag{27}$$

Thereafter, the mixture properties can be found as (Weber et al. 2017; Horstmann et al. 2017; Personnettaz et al. 2018)

$$\begin{gathered} \nu = \frac{1}{\rho} \sum_i \alpha_i \rho_i \nu_i, \quad c_p = \frac{1}{\rho} \sum_i \alpha_i \rho_i c_{p,i}, \\ \lambda = \left(\sum_i \frac{\alpha_i}{\lambda_i} \right)^{-1}, \quad \sigma = \left(\sum_i \frac{\alpha_i}{\sigma_i} \right)^{-1} \quad \text{and} \quad \rho = \sum_i \alpha_i \rho_i. \end{gathered} \tag{28}$$

Note that the kinematic viscosity ν and heat capacity c_p are weighted by density, the thermal conductivity λ and electric conductivity σ harmonically and the density linearly, as illustrated schematically in Fig. 4. Harmonic weighting is especially important for electric conductivity, because its value changes typically by four orders of magnitude between the electrodes and the molten salt.

Surface tension is added as a volumetric force around the interface as

$$\boldsymbol{f} = \sum_i \sum_{j \neq i} \gamma_{ij} \kappa_{ij} \delta_{ij} \tag{29}$$

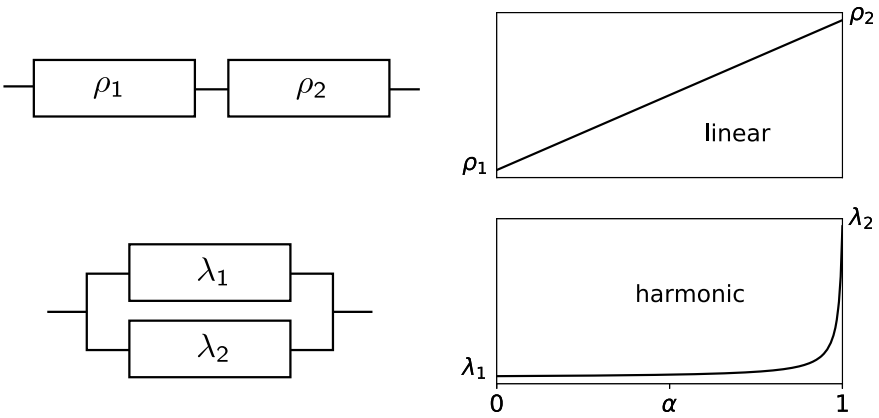

Fig. 4 Densities are weighted linearly like two resistances in a serial circuit, while thermal and electrical conductivities are harmonically weighted as resistivities in a parallel circuit

using the CSF model of Brackbill et al. (1992). Here, γ_{ij} denotes the surface tension between phase i and j with the curvature of the interface defined as

$$\kappa_{ij} = -\nabla \cdot \frac{\alpha_j \nabla \alpha_i - \alpha_i \nabla \alpha_j}{|\alpha_j \nabla \alpha_i - \alpha_i \nabla \alpha_j|}. \tag{30}$$

Finally, the term $\delta_{ij} = \alpha_j \nabla \alpha_i - \alpha_i \nabla \alpha_j$ ensures that the surface tension force is applied only near the interface.

Spurious Velocities

Spurious velocities are unphysical velocities that appear in volume of fluid simulations near the interface—and can easily reach 1 cm/s in LMB simulations, if no countermeasures are taken. Generally, spurious velocities are caused by an imbalance of the pressure gradient with an arbitrary volume force. Typical sources for spurious currents are large density jumps between two phases, a bad curvature calculation and the explicit discretisation of the surface tension force. Very simple measures for reducing spurious currents include lowering the pressure residual, and basing the time step on the capillary Courant number as (Personnettaz et al. 2018)

$$\Delta t = \sqrt{\frac{(\rho_A + \rho_B)\Delta x^3}{2\pi \gamma_{\max}}} \cdot \mathrm{Co}_{\mathrm{cap}}, \tag{31}$$

with ρ_A and ρ_B denoting the densities of two phases, Δx the mesh cell size and $\gamma_{\max}$ the largest interface tension.

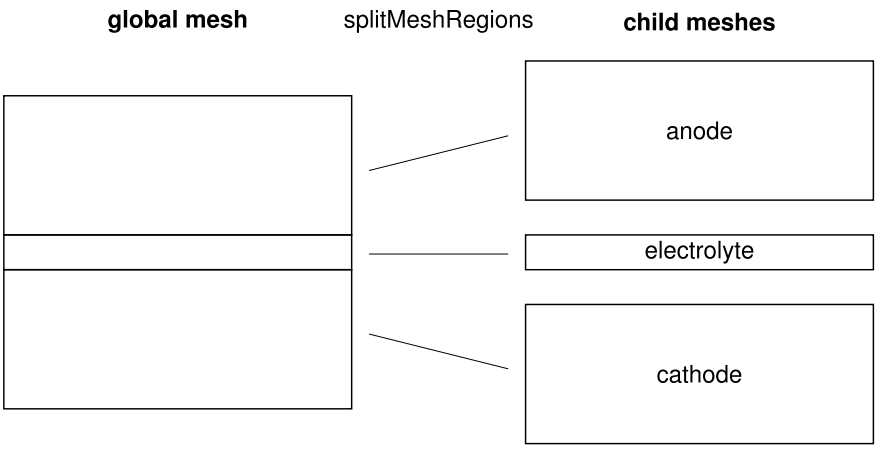

Fig. 5 The OpenFOAM utility splitMeshRegion is used to split the global mesh into several child meshes

3.2 Multi-Region Simulation

When using the multi-region approach, the interfaces between electrodes and electrolyte are assumed to be rigid. Different equations are solved in different regions, e.g. one in the electrode and another in the electrolyte. The meshes are coupled at the boundary, or in the volume by mesh-to-mesh interpolation.

3.2.1 Parent-Child Mesh Method

Certain variables, such as temperature, electric potential or current density, exist in the whole battery. It is therefore opportune to solve them on a global mesh covering all the LMB. Material properties are then simply defined as a *volScalarField* to account for their changes between different conductors.

Distinct from the global mesh, one child mesh is defined for each single region. This allows solving local variables (as e.g. the concentration) in the appropriate region only. Local source terms, such as the heat of reaction, may be mapped easily between child and parent mesh, as both are overlapping.

On a first glance the handling of, and the interpolation between different meshes seems to be complicated. However, the parent-child mesh technique has one important advantage: simulation is fast. Renouncing to the global mesh would require solving e.g. temperature on each region-mesh. This can be very slow, because the fields are only coupled at the boundary. Especially when using explicit coupling, one would need to iterate between the different regions for many times up to convergence.

Still, one notable exception exists: velocity. Solving for velocity and pressure on one global mesh—with rigid boundaries—would require defining an appropriate

coupling for pressure and velocity. As that might be complex, it is better to solve the flow on the child meshes, and couple the velocity at the interfaces.

3.2.2 Mapping Between Meshes

The global mesh is split into child meshes by running the OpenFOAM utility *splitMeshRegions* as illustrated in Fig. 5. This creates three files for each child: faceRegionAddressing, cellRegionAddressing and boundaryRegionAddressing. Here, boundaryRegionAddressing is a simple list, where entry i contains the parent-boundary number which belongs to the child-patch i. Similarly, the entry i in cellRegionAddressing gives the parent-cell number, belonging to child-cell i. The file faceRegionAddressing works similarly, but contains additional information: the orientation of the faces. If an entry of faceRegionAddressing is positive, the parent and child face have the same orientation—otherwise they are inverse. As zero can not have a sign, faceRegionAddressing counts beginning from 1. This means, we obtain the parent-face number of child-face i by

```
label parentFace = mag(fluidFaceRegionAddressing[i]) - 1;
```

and its relative orientation by

```
scalar orientation = sign(fluidFaceRegionAddressing[i]);
```

Within a multi-region solver, we read the three files mentioned above for each child-mesh, and save the mapping information as a cellMap, boundaryMap and faceMap, and the orientation of the faces as a faceMask—for an illustration, see Fig. 6.

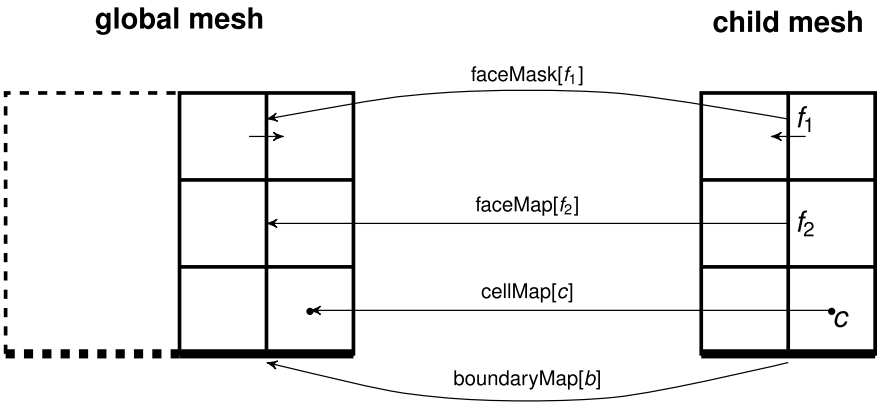

Fig. 6 Mapping between the global and a single child mesh

Child to parent mapping
With this information, cell values can simply be mapped from a child mesh to the parent mesh by invoking

```
globalField.rmap(childField, cellMap);
```

Similarly, patchI can be mapped from the child to the parent-mesh by first defining a local field mapper as

```
labelField tmpMap
(
    labelField::subField
    (
        faceMap,
        childMesh.boundary()[patchI].size(),
        childMesh.boundary()[patchI].patch().start()
    )
);
```

and subtracting then the start index of the parent-patch as

```
tmpMap -= globalMesh.boundary()[patchesMap[patchI]].patch().start();
```

Finally, the boundary field is mapped as

```
globalField.boundaryFieldRef()[patchesMap[patchI]].
      scalarField::rmap(childField.boundaryField()[patchI], tmpMap);
```

Parent to child mapping

Mapping cell values from the parent to a child mesh is similarly easy:

```
forAll(childField, cellI)
{
    childField[cellI] = globalField[cellMap[cellI]];
}
```

Boundary values are mapped analogue as described before by defining a local field mapper, subtracting the start index of the parent mesh and invoking then

```
forAll(childField.boundaryField()[patchI], faceI)
{
    childField.boundaryFieldRef()[patchI][faceI] =
        parentField.boundaryField()[patchesMap[patchI]][tmpMap[faceI]];
}
```

4 Discretisation

The standard discretisation schemes are used for most equations. Only the exceptions are described below: the gradient and Laplace operator for the electric potential, the interpolation of temperature and potential as well as the interpolation of thermal and electrical conductivity need special attention.

4.1 Laplace Operator

When solving the Laplace equation for the electric potential, internal voltage jumps $\Delta\varphi$ need to be accounted for as described in Sect. 2.1. The Laplace operator is discretised using the Gauss theorem as

$$\nabla \cdot \sigma \nabla \varphi = \sum_f \boldsymbol{S}\sigma_\mathrm{f}(\nabla\varphi)_\mathrm{f} = \sum_f |\boldsymbol{S}|\sigma_\mathrm{f}\frac{\varphi_\mathrm{N} - \varphi_\mathrm{P} + \Delta\varphi}{|\boldsymbol{d}|}, \tag{32}$$

where $\boldsymbol{S}$ denotes the face-normal vector, σ_f the conductivity on the face, $(\nabla\varphi)_\mathrm{f}$ the potential gradient on the face, φ_P the potential in the cell centre of the owner cell, φ_N the potential in the cell centre of the neighbour cell and $|\boldsymbol{d}|$ the distance between both cells. Compared to the standard discretisation, only the potential jump $\Delta\varphi$ is added. The jump is defined as a *surfaceScalarField*, which is zero on all faces except at the interface.

4.2 Gradient Operator

The gradient operator for the electric potential needs special attention, because it must account for the jumps at the interfaces. It is discretised as (Jasak 1996)

$$\nabla\varphi = \frac{1}{V}\sum_f \boldsymbol{S}\varphi_\mathrm{f}, \tag{33}$$

with V denoting the cell volume, and the electric potential at the faces defined as

$$\varphi_\mathrm{fP} = w \cdot (\varphi_\mathrm{N} - \Delta\varphi) + (1 - w) \cdot \varphi_\mathrm{P}, \tag{34}$$

and the weighting factor

$$w = \frac{\delta_\mathrm{P} \cdot \sigma_\mathrm{N}}{\delta_\mathrm{N}\sigma_\mathrm{P} + \delta_\mathrm{P}\sigma_\mathrm{N}}. \tag{35}$$

Here, δ_P and δ_N denote the distance between face and cell centre for the owner and neighbour cell, as illustrated in Fig. 7.

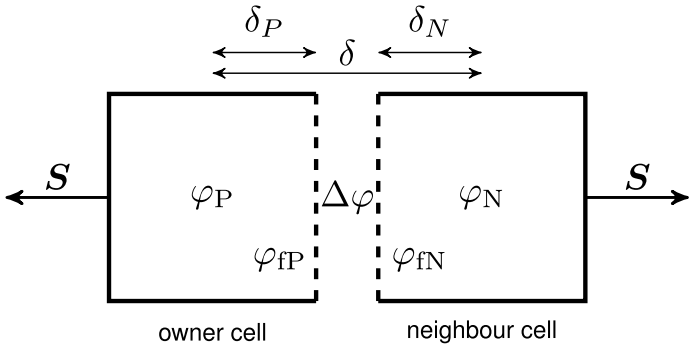

Fig. 7 Discretisation of the electric potential for the Laplace and gradient operator

4.3 Interpolation Schemes

4.3.1 Thermal and Electric Conductivity

When discretising the Laplace equation (Eq. 32), i.e. $\nabla \cdot (\sigma \nabla \varphi) = 0$, the electrical conductivity needs to be interpolated from cell centres to the faces. While linear interpolation can be used for resistance, conductivity needs to be harmonically interpolated as (Weber et al. 2018)

$$\sigma_\mathrm{f} = \frac{1}{\dfrac{w}{\sigma_\mathrm{P}} + \dfrac{1-w}{\sigma_\mathrm{N}}}, \tag{36}$$

with P denoting the owner cell and N the neighbour cell. The weighting factor reads

$$w = \frac{\delta_\mathrm{P}}{\delta_\mathrm{P} + \delta_\mathrm{N}} \tag{37}$$

with δ_P denoting the distance from the cell centre to the face of the owner, and similar for δ_N of the neighbour cell (see Fig. 8).

4.3.2 Temperature and Electric Potential

When computing the current density as $\boldsymbol{j} = -\sigma \nabla \varphi$, the electric potential needs to be interpolated from cell centres to the faces. As the local potential depends strongly

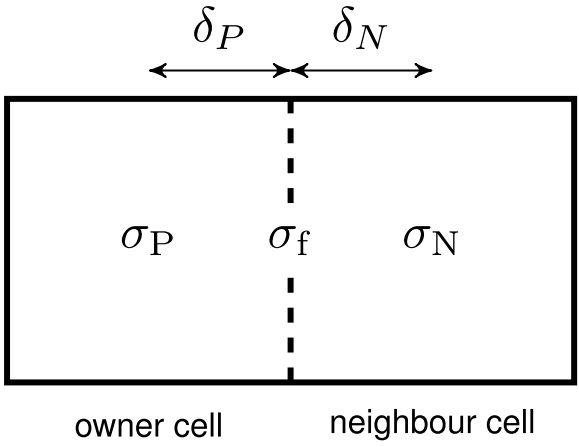

Fig. 8 Interpolation of the electric and thermal conductivity from the cell centres to the faces

on the electric conductivity, the potential needs to be weighted by conductivity when being interpolated. We find the potential at the face as (Weber et al. 2018)

$$\varphi_\mathrm{f} = w\varphi_\mathrm{P} + (1-w)\varphi_\mathrm{N} \tag{38}$$

with

$$w = \frac{\delta_\mathrm{N}\sigma_\mathrm{P}}{\delta_\mathrm{P}\sigma_\mathrm{N} + \delta_\mathrm{N}\sigma_\mathrm{P}}. \tag{39}$$

5 Example

In this section we illustrate the application of our models with a simple example. The corresponding source code is provided with the book. We model the solutal convection in the cathode of an LMB during charge. We solve the Navier-Stokes equation (Eq. 12) for a single fluid with one single body force: the buoyancy due to concentration gradients (Eq. 7). We find the concentration of Li in Bi by solving the diffusion-convection equation (Eq. 6) using Faraday's law as boundary condition (Eq. 8).

During the first three seconds, Li only diffuses out of the electrode (Fig. 9). However, after only 7.5 seconds small fingers of heavy Bi start to sink down reaching the bottom of the cell in only 15 seconds.

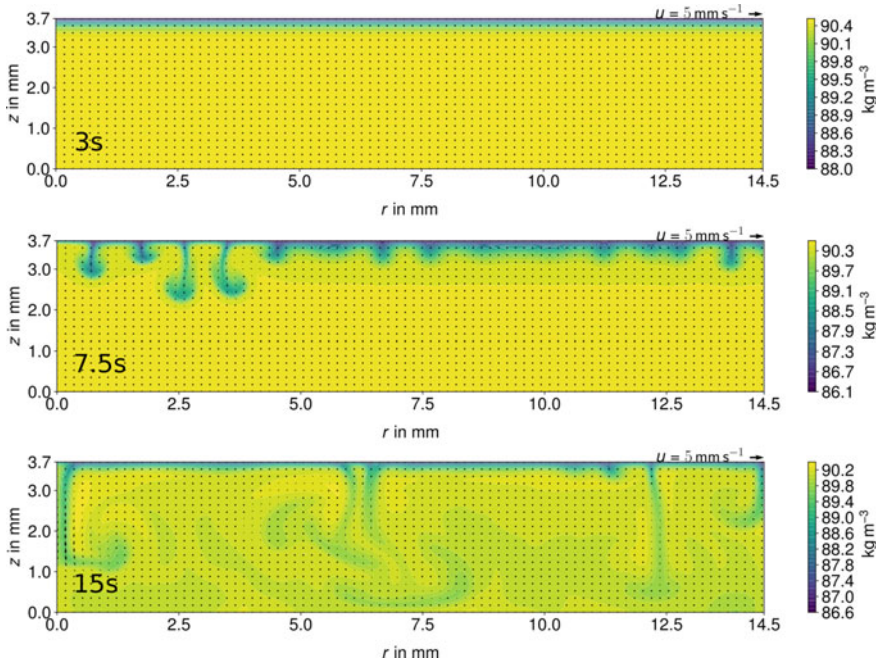

Fig. 9 Mass concentration and velocity vectors in a LiBi cathode during charge of an LMB

Acknowledgements This project has received funding from the European Union's Horizon 2020 research and innovation programme under grant agreement No 963599, and was supported by the Deutsche Forschungsgemeinschaft (DFG, German Research Foundation) by award number 338560565, by a postdoc fellowship of the German Academic Exchange Service (DAAD) and in frame of the Helmholtz—RSF Joint Research Group "Magnetohydrodynamic instabilities: Crucial relevance for large scale liquid metal batteries and the sun-climate connection", contract No. HRSF-0044 and RSF-18-41-06201. We thank P. Personnettaz for providing the source code and example.

References

Ashour RF, Kelley DH, Salas A, Starace M, Weber N, Weier T (2018) Competing forces in liquid metal electrodes and batteries. J. Power Sources 378:301–310

Bird RB, Stewart WE, Lightfoot EN (1960) Transport Phenomena. John Wiley and Sons, New York

Brackbill JU, Kothe DB, Zemach C (1992) A continuum method for modeling surface tension. J. Comput. Phys. 100:335–354

Cairns EJ, Shimotake H (1969) High-temperature batteries. Science 164:1347–1355

Horstmann GM, Weber N, Weier T (2018) Coupling and stability of interfacial waves in liquid metal batteries. *J. Fluid Mech.*, 845:1–35

Gray DD, Giorgini A (1976) The validity of the Boussinesq approximation for liquids and gases. Int. J. Heat Mass Transf. 19(5):545–551

Rusche H (2002) *Computational Fluid Dynamics of Dispersed Two-Phase Flows at High Phase Fractions*. PhD thesis, Imperial College London

Herreman W, Bénard S, Nore C, Personnettaz P, Cappanera L, Guermond J-L (2020) Solutal buoyancy and electrovortex flow in liquid metal batteries. Phys. Rev. Fluids 5(7):074501

Jasak H (1996) *Error Analysis and Estimation for the Finite Volume Method with Applications to Fluid Flows*. PhD thesis, Imperial College of Science, Technology and Medicine

Kelley DH, Weier T (2018) Fluid mechanics of liquid metal batteries. Appl. Mech. Rev. 70(2):020801

Kim H, Boysen DA, Newhouse JM, Spatocco BL, Chung B, Burke PJ, Bradwell DJ, Jiang K, Tomaszowska AA, Wang K, Wei W, Ortiz LA, Barriga SA, Poizeau SM, Sadoway DR (2013) Liquid metal batteries: past, present, and future. Chem. Rev. 113(3):2075–2099

Köllner T, Boeck T, Schumacher J (2017) Thermal Rayleigh-Marangoni convection in a three-layer liquid-metal-battery model. Phys. Rev. E 95:053114

Weber N, Beckstein P, Herreman W, Horstmann GM, Nore C, Stefani F, Weier T (2017) Sloshing instability and electrolyte layer rupture in liquid metal batteries. *Phys. Fluids*, 29(5):054101

Personnettaz P, Landgraf S, Nimtz M, Weber N, Weier T (2019) Mass transport induced asymmetry in charge/discharge behavior of liquid metal batteries. Electrochem. Commun. 105:106496

Personnettaz P, Landgraf S, Nimtz M, Weber N, Weier T (2020) Effects of current distribution on mass transport in the positive electrode of a liquid metal battery. Magnetohydrodynamics 56(2/3):247–254

Personnettaz P, Beckstein P, Landgraf S, Köllner T, Nimtz M, Weber N, Weier T (2018) Thermally driven convection in Li||Bi liquid metal batteries. J. Power Sources 401:362–374

Shen Y, Zikanov O (2016) Thermal convection in a liquid metal battery. Theor. Comput. Fluid Dyn. 30(4):275–294

Weber N, Galindo V, Stefani F, Weier T (2015) The Tayler instability at low magnetic Prandtl numbers: Between chiral symmetry breaking and helicity oscillations. New J. Phys. 17(11):113013

Weber N, Galindo V, Stefani F, Weier T, Wondrak T (2013) Numerical simulation of the Tayler instability in liquid metals. New J. Phys. 15:043034

Weber N, Landgraf S, Mushtaq K, Nimtz M, Personnettaz P, Weier T, Zhao J, Sadoway D (2019) Modeling discontinuous potential distributions using the finite volume method, and application to liquid metal batteries. Electrochim. Acta 318:857–864

Weber N, Nimtz M, Personnettaz P, Salas A, Weier T (2018) Electromagnetically driven convection suitable for mass transfer enhancement in liquid metal batteries. Appl. Therm. Eng. 143:293–301

Weber N, Nimtz M, Personnettaz P, Weier T, Sadoway D (2020) Numerical simulation of mass transfer enhancement in liquid metal batteries by means of electro-vortex flow. J. Power Sources Advances 1:100004

Weber N, Beckstein P, Galindo V, Starace M, Weier T (2018) Electro-vortex flow simulation using coupled meshes. Comput. Fluids 168:101–109

Weier T, Bund A, El-Mofid W, Horstmann GM, Lalau C-C, Landgraf S, Nimtz M, Starace M, Stefani F, Weber N (2017) Liquid metal batteries—materials selection and fluid dynamics. IOP Conf. Ser. Mater. Sci. Eng. 228:012013